

Article

Evaluating Superconductors through Current Induced Depairing

Milind N. Kunchur

Department of Physics and Astronomy, University of South Carolina, Columbia, SC 29208, USA; kunchur@sc.edu; Tel.: +1-803-777-1907

Received: 22 May 2019; Accepted: 15 June 2019; Published: 17 June 2019

Abstract: The phenomenon of superconductivity occurs in the phase space of three principal parameters: temperature T , magnetic field B , and current density j . The critical temperature T_c is one of the first parameters that is measured and in a certain way defines the superconductor. From the practical applications point of view, of equal importance is the upper critical magnetic field B_{c2} and conventional critical current density j_c (above which the system begins to show resistance without entering the normal state). However, a seldom-measured parameter, the depairing current density j_d , holds the same fundamental importance as T_c and B_{c2} , in that it defines a boundary between the superconducting and normal states. A study of j_d sheds unique light on other important characteristics of the superconducting state such as the superfluid density and the nature of the normal state below T_c , information that can play a key role in better understanding newly-discovered superconducting materials. From a measurement perspective, the extremely high values of j_d make it difficult to measure, which is the reason why it is seldom measured. Here, we will review the fundamentals of current-induced depairing and the fast-pulsed current technique that facilitates its measurement and discuss the results of its application to the topological-insulator/chalcogenide interfacial superconducting system.

Keywords: vortex; vortices; theory

The phenomenon of superconductivity has a long and rich history: from the initial discovery in 1911 of superconductivity in mercury at liquid-helium temperature [1] to the recent discovery of room-temperature superconductivity in lanthanum superhydride [2,3]. Numerous parameters, probed by a variety of techniques, are used to characterize the superconducting state. However, the mixed-state upper critical field B_{c2} , reflective of the coherence length ξ , and the penetration depth λ_L , reflective of the superfluid density $\rho_s = 1/\lambda^2$, are two crucial measurements that are amongst the first to be performed. There are multiple techniques for determining such parameters, each of which has its own advantages and limitations. Our group has developed some uncommon, and in some cases unique, experimental techniques that investigate superconductors at ultra-short time scales, and under unprecedented and extreme conditions of current density j , electric fields E , and power density $p = \rho j^2$ (where ρ is the resistivity). These techniques have led to the discovery or confirmation of several novel phenomena and regimes in superconductors and in addition provide an alternative method to glean information on fundamental superconducting parameters, which in some cases may be hard to obtain by other methods. These methods and approaches are highly relevant in the search for new superconducting materials and in developing an understanding of their fundamental properties. This article discusses the physical meaning of j_d and its interrelationships with other basic parameters of the superconducting state, as well as the technical challenges in measuring this important critical parameter. We discuss our results from this approach in the study of the topological-insulator/chalcogenide interfacial superconducting system.

1. Introduction

Attractive interactions between charge carriers cause them to condense by pairs into a coherent macroscopic quantum state below some transition temperature T_c . The formation of this state is governed principally by a competition between four energies: condensation, magnetic-field expulsion, thermal, and kinetic. The order parameter Δ , which describes the extent of condensation and the strength of the superconducting state, is reduced as the temperature T , magnetic field B , and electric current density j are increased. In type-II superconductors, there is partial flux entry at B values above the lower critical magnetic field B_{c1} and complete destruction of superconductivity above the upper critical field B_{c2} (type-I superconductors can be viewed as a special case where the thermodynamic critical field $B_c = B_{c1} = B_{c2}$). The boundary in the T - B - j phase space that separates the superconducting and normal states is where Δ vanishes, and the three parameters attain their critical values $T_{c2}(B, j)$, $B_{c2}(T, j)$, and $j_d(T, B)$. j_d sets the intrinsic upper limiting scale for supercurrent transport in any superconductor, and for $j > j_d$, the system attains its normal-state resistivity ρ_n . j_d should be distinguished from the conventional critical value j_c (related to intrinsic characteristics such as the depinning of vortices) above which there is partial resistivity $\rho < \rho_n$.

The resistivity ρ in the superconducting state is usually less than its normal-state value ρ_n . The reason for the presence of resistance at all in the superconducting state is because of fluctuations, percolation through junctions (in the case of granular superconductors), and the motion of magnetic flux vortices. For singly-connected superconductors not very close to T_c , only the last mechanism dominates as the cause of resistance. In the magnetic field region between B_{c1} and B_{c2} , a type II superconductor enters a “mixed state” with quantized magnetic flux vortices, each containing an elementary quantum of flux $\Phi_0 = h/2e$. Under the Lorentz driving force of an applied current, $\mathbf{j} \times \Phi_0$, vortices move transverse to j , leading to a flux-flow resistivity:

$$\rho_f \sim \rho_n B / B_{c2} \tag{1}$$

in the free-flux-flow (large driving force) limit.

Two length scales characterize the superconducting state [4]. One is the coherence length:

$$\xi = v_F \tau_\Delta \simeq \hbar v_F / \pi \Delta \tag{2}$$

which is the characteristic length scale for spatial modulations in Δ (here, v_F is the Fermi velocity and τ_Δ is the order-parameter relaxation time). The normal core of a flux vortex has an approximate effective radius of ξ . The destruction of the superconducting state occurs when these normal cores overlap, corresponding to the condition:

$$B_{c2} = \frac{\Phi_0}{2\pi\xi^2} = \frac{\Phi_0}{2\pi\xi_1\xi_2} \tag{3}$$

where ξ is the coherence length perpendicular to B ; the single ξ is replaced by the geometric mean $\sqrt{\xi_1\xi_2}$ in cases where the plane perpendicular to B is characterized by two anisotropic values.

The other characteristic length scale in a superconductor is the magnetic-field penetration depth λ , whose London value is given by:

$$\lambda_L = \sqrt{\frac{m^*}{\mu_0 n_s e^2}} \tag{4}$$

where m^* is the effective electronic mass and n_s is the density of superconducting electrons. The theory behind this important quantity and its relationship to j_d is described below. Figure 1 shows the profile of the magnetic field as it gets screened from the interior of a superconductor.

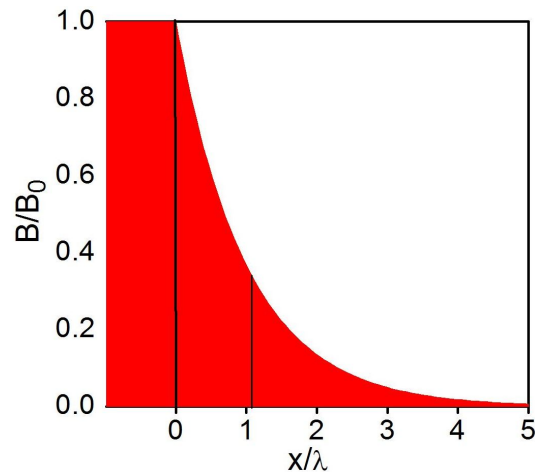


Figure 1. An externally-applied magnetic field B_0 is screened from the interior of a superconductor in the Meissner state over a characteristic length scale, which is the magnetic-field penetration depth λ : $B \sim B_0 e^{-x/\lambda}$. The circulating screening current is of roughly the depairing magnitude j_d , so that $\lambda \propto 1/j_d$.

1.1. Superfluid Density

For clean metallic superconductors, $n_s \rightarrow n$ as $T \rightarrow 0$, where n is the concentration of carriers in the normal state. Non-local effects and other corrections lead to deviations in λ from its London value. Hence, the superfluid density ρ_s can be conveniently and more completely defined as:

$$\rho_s \equiv 1/\lambda^2 \tag{5}$$

which includes the effective mass and other corrections to the effective n_s , rather than the simpler definitions $\rho_s = n_s$ or $\rho_s = n_s/m^*$ that are sometimes used in the literature. ρ_s , a quantity of central importance in superconductivity, characterizes the phase stiffness of the condensate [5] and its effectiveness at screening out magnetic fields and feeds into expressions for the transition temperature (such as the Uemura relation $T_c \propto \rho_s(0)$ that applies to the underdoped cuprate superconductors [6–8]).

Traditionally, many common methods for obtaining ρ_s do so by directly or indirectly measuring λ through its effect on a superconducting sample’s magnetic-field profile and consequent magnetic susceptibility. This category includes methods such as reflection of spin-polarized slow neutrons [9], mutual inductance altered by an intervening superconducting film [10,11], changes in the self-inductance of a coil that is part of an LC resonating circuit [12,13], muon-spin rotation [14], magnetic force microscopy [15], microwave cavity resonance [16], and measurements of the lower critical field. These measurements are understandably affected if the material’s internal magnetic field is altered, for example by a large paramagnetic background as in the case of the $\text{Nd}_{2-x}\text{Ce}_x\text{CuO}_4$ superconductor because of its Nd^{3+} magnetic moments.

Another approach to obtaining ρ_s is by measuring the inertia of the superfluid (kinetic inductance) during its ballistic acceleration phase [17–20]. This method requires the sample to be patterned into very high aspect ratio meanders for the highest accuracy.

A measurement of j_d provides an alternative to the above approaches for obtaining ρ_s . It requires a minimal amount of material (typically just a microbridge or nanobridge), does not require the complicated meander patterning needed for a kinetic-inductance measurement, and is unaffected by a material’s normal-state magnetism that affects inductive measurements of ρ_s as discussed above. This immunity to material magnetism was used to good advantage for directly obtaining ρ_s in the $\text{Nd}_{2-x}\text{Ce}_x\text{CuO}_4$ superconductor for the first time [21]. Furthermore, unlike some of the methods for measuring λ that do not provide an accurate absolute value but only provide the temperature variation

$\lambda(T)/\lambda(0)$, j_d does provide the absolute value of λ and ρ_s and can hence provide information on the total carrier concentration n .

1.2. Normal-State Resistivity

Another valuable byproduct of measuring j_d is that it provides a direct measurement of the normal state resistivity ρ_n for temperatures below T_c . One of the starting points in developing an understanding of any newly-discovered superconductor is to understand the underlying normal state: the type of carriers and their concentration, their band-related properties, and the relevant scattering mechanisms and rates. At low applied B and j , $\rho(T)$ drops precipitously below T_c , thereby obscuring how $\rho_n(T \ll T_c)$ would have behaved if the superconductivity had not set in. The most common method for measuring $\rho_n(T < T_c)$ utilizes high magnetic fields $B > B_{c2}$ to drive the system normal below T_c ; however, this measurement is subject to magnetoresistance (typically $R(B) \neq \text{const}$) and may require prohibitively high magnetic fields ($B_{c2} > 100$ T for some superconductors).

One alternative is to use the core of a magnetic flux vortex as a window to the normal state. From Equation (1), a measurement of ρ_f elucidates ρ_n [22]. However, this extraction of ρ_n requires interpretation and modeling, since Equation (1) usually holds only approximately except for very high driving forces, and the exact prefactor depends on the detailed regime of flux flow [23–25].

Current-induced depairing provides an especially clean method for destroying superconductivity and accessing $\rho_n(T \ll T_0)$. Like the method of applying $B > B_{c2}$ to drive the system normal, applying $j > j_d$ is also free of interpretation and modeling, unlike flux-flow dissipation measurements. On the other hand, unlike the potential errors in the B_{c2} -based measurement due to normal-state magnetoresistance, the j_d method is immune to this issue because the normal-state electroresistance is quite negligible (i.e., $R(E) \simeq \text{const}$) under the electric fields that arise at depairing conditions.

Thus, besides the investigation of interesting phenomena and regimes in superconductivity related directly to current-induced depairing itself, the study of j_d provides information on the important parameters of the superconducting state such as $\rho_s(T)$ and $\rho_n(T)$.

2. Relationship between the Depairing Current and Other Parameters

In a microscopic theory such as the Bardeen–Cooper–Schrieffer (BCS) theory, experimental quantities are calculated from microscopic parameters such as the strength of the effective attractive interaction that leads to Cooper pair formation and the density of states at the Fermi level. Often, these microscopic parameters are not sufficiently well known. In the London and Ginzburg–Landau (GL) phenomenological theories, connections are made between the different observables from constraints based on thermodynamic principles and electrodynamic properties of the superconducting state, leading to an adequate estimation of the depairing current. These phenomenological formulations are described next [4,26].

2.1. London Formulation

The London theory [4,27] of superconductivity provides a description of the observed electrodynamic properties by supplementing the basic Maxwell equations by additional equations that constrain the possible behavior to reflect the two hallmarks of the superconducting state: perfect conductivity and the Meissner effect. Note that these properties hold only partially when vortices are present.

An ordinary metal (normal conductor) requires a driving electric field E to maintain a constant current against resistive losses. In the simple Drude picture, this produces Ohm's law behavior, $j = \sigma E$, with a conductivity given by $\sigma = ne^2\tau/m^*$. A superconductor can carry a resistanceless current, and so,

an electric field is not required for maintaining a persistent current. Instead, E in a perfectly-conducting state causes a ballistic acceleration of charge so that:

$$E = \left(\frac{m^*}{n_s e^2} \right) \frac{\partial j}{\partial t} \tag{6}$$

This is the first London equation, which reflects the dissipationless acceleration of the superfluid.

The second property that needs to be accounted for is the expulsion of magnetic flux by a superconductor. The magnetic field is exponentially screened from the interior following a spatial dependence:

$$\nabla^2 B = B / \lambda_L^2 \tag{7}$$

Together with the Maxwell equation $\nabla \times B = \mu_0 j$, this implies the following condition between B and j :

$$B = -\mu_0 \lambda_L^2 (\nabla \times j) \tag{8}$$

This is the second London equation, which describes the property of a superconductor to exclude magnetic flux from its interior. Taken together with the Maxwell equation $\nabla \times E = -\partial B / \partial t$, Equations (6) and (8) yield the expression for λ_L of Equation (4).

Besides the London equations themselves, a third ingredient needed for the estimation of j_d in this framework is the thermodynamic critical field B_c and its relationship to the Helmholtz free energy density f . When flux is expelled, the free energy density is raised by the amount $B^2 / 2\mu_0$. The critical flux expulsion energy (for the ideal case of a type-I superconductor with a non-demagnetizing geometry and dimensions large compared to the penetration depth) corresponds to the condition:

$$f_c = f_n - f_s = \frac{B_c^2}{2\mu_0} \tag{9}$$

where the L.H.S. of the equation represents the condensation energy density, which is the difference in free energy densities $f_n - f_s$ between the normal and superconducting states. j_d represents the condition when the kinetic energy density equals the condensation energy density: $\frac{1}{2} n_s m^* v_s^2 = \frac{m^* j_d^2}{2n_s e^2} = \frac{B_c^2}{2\mu_0}$, where v_s is the superfluid speed. Substituting for λ_L (Equation (4)) gives the London estimate for the depairing current density:

$$j_d \leq \frac{B_c}{\mu_0 \lambda_L} \tag{10}$$

The inequality reflects the fact that n_s does not remain constant, but diminishes as j approaches j_d .

2.2. Ginzburg–Landau Formulation

There are situations where a system’s quantum wavefunction cannot be solved for by usual means because the Hamiltonian is unknown or not easily approximated. The GL formulation [28] is a clever construction that allows useful information and conclusions to be extracted in such a situation where one cannot solve the problem quantum mechanically. For describing macroscopic properties, such as j_d that we are about to calculate, the GL theory is in fact more amenable than the microscopic theory [4,29].

The idea is to introduce a complex phenomenological order parameter (pseudo wavefunction) $\psi = |\psi| e^{i\varphi}$ to represent the superconducting state. $|\psi(r)|^2$ is assumed to represent the order parameter Δ introduced earlier, and to approximate the local density of paired superconducting charge carriers (Cooper pairs), which in turn is half the density of superconducting electrons n_s .

The free energy density f_s of the superconducting state is then expressed as a reasonable function of $\psi(r)$ plus other energy terms. A “solution” to $\psi(r)$ is now obtained by the minimization of free energy rather than through quantum mechanics. The unknown parameters of the theory are then

solved in terms of measurable physical quantities, thereby providing constraints between the different quantities of the superconducting state.

Close to the phase boundary, $|\psi|^2$ is small, and so, f_s can be expanded keeping the lowest two orders of $|\psi|^2$. First, let us consider the simplest situation where there are no currents, gradients in $|\psi|$, or magnetic fields present. Then, we have:

$$f_s = f_n + \alpha|\psi|^2 + \frac{\beta}{2}|\psi|^4, \tag{11}$$

where α and β are temperature-dependent coefficients whose values are to be determined in terms of measurable parameters. The coefficients can be determined as follows. First of all, for the solution of $|\psi|^2$ to be finite at the minimum free energy, β must be positive. Second, for the solution of $|\psi|^2$ to be non-zero, α must be negative. Since $|\psi|^2$ vanishes above T_c , α must change its sign upon crossing T_c . The minimum in f_s occurs at:

$$|\psi|^2 = -\alpha/\beta. \tag{12}$$

Substituting this back in Equation (11) and using the definition of B_c (Equation (9)), Equation (12) can be written as:

$$f_c = \frac{B_c^2}{2\mu_0} = \frac{\alpha^2}{2\beta} \tag{13}$$

giving one of the connections between α and β and a measurable quantity (B_c). A second connection can be obtained by noting that n_s in Equation (4) can be replaced by $2|\psi|^2$, taking its equilibrium value from Equation (12):

$$\lambda^2 = \frac{m^*}{2\mu_0|\psi|^2e^2} = \frac{-\beta}{\alpha} \left(\frac{m^*}{2\mu_0e^2} \right) \tag{14}$$

Solving Equations (13) and (14) simultaneously gives the GL coefficients:

$$\alpha = -\frac{2e^2B_c^2\lambda^2}{m^*} \quad \text{and} \quad \beta = \frac{4\mu_0e^4B_c^2\lambda^4}{m^{*2}} \tag{15}$$

Note that e and m^* refer to single-carrier values and not pair values.

To calculate j_d , we include the effect of a current in Equation (11) by adding a kinetic energy term $\frac{1}{2}n_s m^* v_s^2 = |\psi|^2 m^* v_s^2$ to it:

$$f_s = f_n + \alpha|\psi|^2 + \frac{\beta}{2}|\psi|^4 + |\psi|^2 m^* v_s^2. \tag{16}$$

For zero j and v_s , we saw earlier (Equation (12)) that the equilibrium value of $|\psi|^2$ that minimizes the free energy is $|\psi_{j=0}|^2 = -\alpha/\beta$. For a finite j and v_s , minimization of Equation (16) gives the value of $|\psi|^2$ when it is suppressed by a current:

$$|\psi_{j \neq 0}|^2 = \frac{-\alpha}{\beta} \left(1 - \frac{m^* v_s^2}{|\alpha|} \right) = |\psi_{j=0}|^2 \left(1 - \frac{m^* v_s^2}{|\alpha|} \right) \tag{17}$$

The corresponding supercurrent density is then:

$$j = 2e|\psi_{j \neq 0}|^2 v_s = \frac{-2e\alpha}{\beta} \left(1 - \frac{m^* v_s^2}{|\alpha|} \right) v_s \tag{18}$$

The maximum possible value of this expression can now be identified with j_d :

$$j_d(T) = \frac{-4e\alpha}{3\beta} \left(\frac{|\alpha|}{3m^*} \right)^{1/2} = \left(\frac{2}{3} \right)^{3/2} \frac{B_c(T)}{\mu_0\lambda(T)} \tag{19}$$

where the GL-theory parameters were replaced by their expressions in terms of the physical measurables B_c and λ through Equation (15). As anticipated at the end of Equation (10) for the

London derivation for j_d , that simpler estimate is indeed larger than this more rigorous GL derivation by the factor $(3/2)^{3/2} = 1.84$.

The approximate temperature dependence of j_d can be obtained by inserting the generic empirical temperature dependencies $B_c(T) \approx B_c(0)[1 - (T/T_c)^2]$ and $\lambda(T) \approx \lambda(0)/\sqrt{[1 - (T/T_c)^4]}$, giving:

$$j_d(T) \approx j_d(0)[1 - (T/T_c)^2]^{\frac{3}{2}}[1 + (T/T_c)^2]^{\frac{1}{2}} \quad (20)$$

which close to T_c reduces to:

$$j_d(T) \approx \sqrt{2}j_d(0)[1 - (T/T_c)^2]^{\frac{3}{2}}. \quad (21)$$

where $j_d(0)$ is given by Equation (19) by setting $T = 0$ (for high scattering “dirty” superconductors, the $\sqrt{2}$ prefactor can be smaller or absent [29,30]).

Since B_c is not an easy quantity to measure directly, the relation:

$$B_c = \sqrt{\frac{\Phi_0 B_{c2}}{4\pi\lambda^2}} \quad (22)$$

can be used along with Equation (19) to write the expression for $j_d(0)$:

$$j_d(0) = \sqrt{\frac{2\Phi_0 B_{c2}(0)}{27\pi\mu_0^2\lambda^4(0)}} \quad (23)$$

that has the more easily measurable B_{c2} . Since both B_{c2} and j_d can be obtained from transport measurements, this becomes a convenient way to obtain λ and, hence, ρ_s .

2.3. Microscopic Formulations and Generalizations

Various authors have calculated $j_d(T)$ from a microscopic basis [29,31,32]. For arbitrary temperatures and mean free paths, one must use the Gorkov equations as the starting point. Kupriyanov and Lukichev [33] have derived $j_d(T)$ from the Eilenberger equations, which are a simplified version of the Gorkov equations. This derivation is beyond the scope of the present review, but a nice shortened version can be found in [30]. The microscopic calculation confirms the overall temperature dependence predicted by GL, and the two normalized curves differ only slightly from each other (e.g., see Figure 4 of [30]). Thus, the GL theory can be applied over the entire temperature range down to $T \ll T_c$. The previous equations relating j_d to B_c and λ are expected to hold in the case of multiple bands and other gap symmetries, as long as one uses the actual empirical temperature dependencies of B_c and λ , which account for modifications in these unconventional cases. This was experimentally demonstrated in the case of MgB_2 [26], which was recognized as a multi-gap superconductor tuned by strain and doping in the early part of this century; in fact, MgB_2 showed superconductivity near a Lifshitz transition as in iron-based superconductors [34–36].

3. Pulsed Measurement Technique

Depairing current densities in superconductors is extremely high: on the order of $j_d(T = 0) = 10^{11}\text{--}10^{13}$ A/m². If the cross-section of the sample is even as narrow as just 1 mm², the current required would reach a value of $I = jA \sim 10^6$ A. Such a magnitude of current would be exceedingly difficult to produce and control. There are three steps to overcoming this dilemma: (1) Fabricate samples with very narrow cross-sectional areas. This can be achieved by growing nanowires and nanorods or by depositing very thin films and using lithography to pattern narrow bridges (alternatively, the films can be deposited onto nanowires or carbon nanotubes). (2) The next step is by pulsing the current at very low duty cycles so that large values of I can be handled while reducing the time-averaged current and time-averaged power dissipation to manageable levels. (3) The last step is limiting the measurement of j_d to the regime close to T_c . From Equation (21), it would seem that j_d can be made arbitrarily small by making T very close to T_c ;

however, the $T - T_c$ distance needs to be large compared to the transition width for the measurement to be meaningful. Even for this near- T_c measurement of j_d , the current usually will have to be pulsed to avoid significant sample heating. Furthermore, the near- T_c measurement will only measure ρ_s in that region, and its zero- T value will have to be extrapolated using theory. While this is better than nothing, it will not shed light on any abnormal temperature dependence of ρ_s over the entire range, which could be of special interest if the superconductor has some exotic behavior.

Thus, the experimental ingredients needed to conduct a j_d measurement are: a superconducting sample with a very narrow cross-section; a means to control the temperature, i.e., a cryostat; and a method for sourcing pulsed signals (current or voltage) and detecting the consequent complementary signal (voltage or current). There are numerous methods for sample fabrication, which vary widely with the different superconducting materials. Some deposition systems for preparing superconducting films can be bought off the shelf. Cryostats also represent standard equipment that can be bought off the shelf. The principal distinguishing the experimental capabilities of our work center on the pulsed electrical measurements. Therefore, the rest of the experimental section will be devoted to describing this unique measurement setup.

Figure 2 shows the overall configuration and functional schematic. The pulsed current/voltage source puts out a time-varying current and voltage. This signal flows through a standard impedance, usually a resistor R_{std} (although an inductor is preferable in some situations) and the superconducting sample of resistance R that are in series. The initial signal can be taken directly from the output of a standard pulse generator (one of the models used was a Wavetek Model 801). These signal generators will typically have an output impedance of $Z_{out} = 50 \Omega$. If a lower Z_{out} is desirable (to allow for constant voltage control), the signal generator's output can be passed through any standard buffer amplifier (e.g., a transistor-emitter-follower-based circuit, a power-operational-amplifier-based circuit, or an off-the-shelf audio amplifier). If a higher voltage than the signal generator's output is desirable, its output can be passed through any standard voltage amplifier (fast high quality audio amplifiers can serve this purpose as well). Combining a higher voltage signal with a large series resistor (which can be the R_{std} itself or an additional series resistor) can provide a relatively constant current. In general, the measurement will be in current-controlled or voltage-controlled mode depending on whether the combination of the final Z_{out} (after the amplifier if any) plus R_{std} is greater than or less than R . If the current needs to be held constant to a high accuracy (for example, if a series of R vs. T resistive transition curves needs to be traced out at various constant currents, as will be seen later), then it is better to follow the pulse generator with a transconductance amplifier, which converts the generator's voltage pulse into a constant current pulse. The transconductance amplifier is able to hold the current constant by electronic circuitry instead of needing an enormous series resistance. While conducting a pulsed current-voltage (IV) curve, which is usually done manually, it is preferable to have the voltage-controlled mode. The reason for this is that as the current and voltage are pushed higher, the sample's resistance will increase, and at some point, the sample will be driven to normal as j_d is exceeded. In constant-current mode, the power dissipation $P = I^2R$ rises as R rises, causing an increase in heating and a further rise in R . This can lead to a run-away condition, which can destroy the sample. On the other hand, the constant-voltage mode is self-stabilizing since in this case, $P = V^2/R$ decreases as R rises, thus reducing heating and controlling the situation.

Once the current pulse flows through the sample and R_{std} , the corresponding time-varying voltages, $V(t)$ and $V_{std}(t)$, will be developed across them respectively. These must be observed and quantified using an oscilloscope. A digital storage oscilloscope (DSO) allows multiple pulses to be averaged. Since the signal is exactly repetitive, because the DSO is triggered off of the pulse generator's sync signal, the averaging effectively suppresses random uncorrelated noise. As long as the sample condition (T , B , etc.) is stable, a very high number of averages can be taken to improve the signal-to-noise ratio (SNR) vastly. Coaxial cables with 50-Ohm characteristic impedance are used between all connection points, including the wiring within the cryostat. Where possible, the originating and/or terminating points at the ends of the cables need to have matching 50-Ohm values to avoid

reflections. Multiple ground connections to the circuit must be avoided to prevent ground loops. This means the two channels of the DSO cannot be simultaneously connected to both the sample and R_{std} ; either a differential instrumentation preamplifier (Princeton Applied Research and Stanford Research Systems are two brands that make instrumentation amplifiers) must be used between the DSO channels and the sample and R_{std} , or only one of the two must be measured at a time.

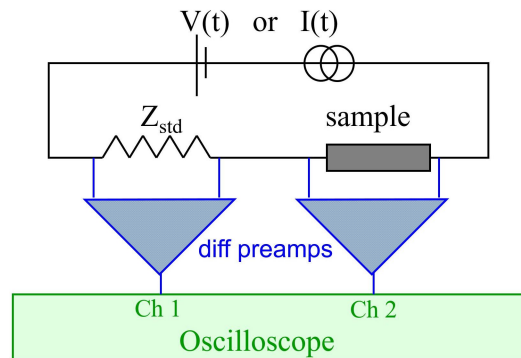


Figure 2. The overall configuration and functional schematic of the pulsed-signal measurement system. The differential preamplifiers (diff preamps) convert the time-varying potential differences across standard impedance (Z_{std}) and the sample, $V_{std}(t)$ and $V(t)$ respectively, into ground referenced single-ended signals that can be fed to the inputs of a digital storage oscilloscope.

Figure 3 shows the pair of time-varying current $I(t) = V_{std}(t)/R_{std}$ and sample-voltage $V(t)$ signals that results. The topmost trace is the scaled calculated resistance $50R(t) = 50V(t)/I(t)$. Note that the pulses reach constant plateaus after their initial transients. R , V , and I are defined by taking the plateau values of the individual quantities. The thermal rise in a sample because of Joule heating involves several processes: thermal diffusion occurs within the sample essentially instantaneously; on the time scale of nanoseconds, phonons transfer heat across the interface between the film and substrate; heat then diffuses within the substrate in a matter of microseconds and finally into the heat sink in milliseconds. For those processes that have time scales comparable to or longer than the pulse duration, there will be a visible rise in $V(t)$, causing the pulse to be distorted. Thus, as long as the $V(t)$ pulse is flat, slow causes of heating that influence the $V(t)$ shape can be assumed to be negligible. The work in [37] discusses a method to evaluate a sample’s thermal resistance for pulsed signals quantitatively.

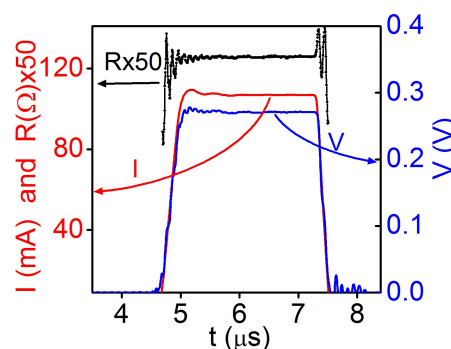


Figure 3. The measured oscilloscope traces of the sample voltage $V(t)$, current $I(t) = V_{std}(t)/R_{std}$, and scaled calculated resistance $50R(t) = 50V(t)/I(t)$ for an MgB_2 bridge at 42 K (normal state just above T_c). The resistance rises from 10–90% of its final value in about 50 ns (adapted from Reference [26]).

Figure 4 shows an example [26] of a set of IV curves at various fixed temperatures (in zero magnetic field), where each data point represents a pulsed measurement (plateau values) as described

above. As the temperature is increased, j_d is reduced, and hence, the “jump” occurs at a lower value of I . Notice that the resistance (the V/I slope) jumps from zero (dissipationless superconducting state) to a constant finite value (normal-state) as the current crosses its depairing value. This is one direct way of obtaining ρ_n below T_c . In this particular material, high impurity scattering dominates over electron-phonon scattering at all temperatures, leading to a relatively flat $\rho(T)$. A more interesting application of this technique for elucidating a variable $\rho(T)$ is described in a later section.

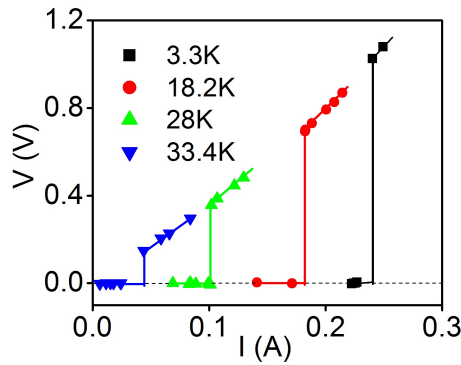


Figure 4. Current-voltage curves in a MgB₂ bridge at various fixed temperatures. As the temperature is increased, j_d is reduced, and hence, the “jump” occurs at a lower value of I . The sloped portions above each jump represent the normal-state resistance $R_n = \Delta V / \Delta I$ (adapted from Reference [26]).

Figure 5a represents a set of pulsed constant-current $R(T)$ curves in zero magnetic field [38]. As the current is increased, the transition is progressively pushed down in temperature. Figure 5b plots these midpoint transition temperatures (T_{c2}) versus I , and they are seen to follow a $I^{2/3}$ law as per Equation (21). From this measured slope and Equation (21), one can estimate $j_d(0)$ without requiring the application of this enormous value of current. This is especially useful for systems (e.g., cuprate high-temperature superconductors) that have a very high $j_d(0)$ value.

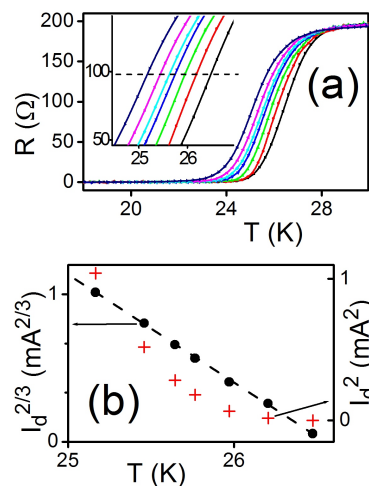


Figure 5. (a) Resistive transitions in a Sr_{1-x}La_xCuO₂ superconducting film bridge in zero magnetic field at various transport current values (right to left): 12.9, 132, 258, 426, 533, 721, and 1020 μ A. The lowest current is continuous DC; the remaining currents are pulsed. The inset shows a magnified view of the midpoint region. (b) Left axis (circle symbols): two-thirds power of the depairing current versus the midpoint transition temperature corresponding to the depairing law. Right axis (plus symbols): square of the depairing current versus the midpoint transition temperature corresponding to Joule heating (adapted from Reference [38]).

Figure 6 shows the companion very low DC-current $R(T)$ curves at various constant B values. Here, the shift occurs because of the $B_{c2}(T)$ boundary; the current level is small enough for its depairing to be negligible. Unlike $j_d(T)$, $B_{c2}(T)$ has a linear dependence near T_c , and that slope can be related to $B_{c2}(0)$ through the WHH (Werthamer, Helfand, and Hohenberg) theory [39] and its variations [40] by relationships such as $B_{c2}(0) \simeq 0.7d B_{c2}/dT$.

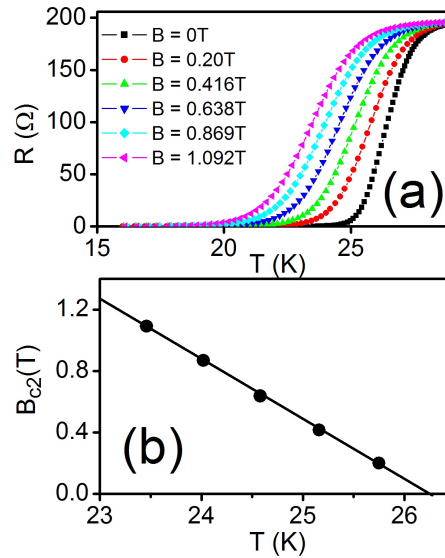


Figure 6. (a) Resistive transitions of a $\text{Sr}_{1-x}\text{La}_x\text{CuO}_2$ superconducting film bridge at a constant current of $I = 13 \mu\text{A}$ in various perpendicular magnetic field values as indicated in the key. (b) Upper critical magnetic field versus the midpoint transition temperature, extracted from the curves in (a) (adapted from Reference [38]).

The measurements represented by Figures 5 and 6 together with Equation (23) are the key to obtaining ρ_s through relatively straightforward transport measurements. We now look at one recent example of a current-induced depairing study of an exotic superconducting system.

4. Investigations in a Topological Insulator/Chalcogenide Interfacial Superconductor

4.1. Background

The interface between the Bi_2Te_3 topological insulator and the FeTe chalcogenide provides a fascinating 2D superconducting system, in which neither Bi_2Te_3 , nor FeTe are superconducting by themselves [41]. While the exact origin of the superconductivity is not known, it has been suggested that the robust topological surface states may be doping the FeTe and suppressing the antiferromagnetism in a thin region close to the interface, thus inducing the observed 2D superconductivity. These surface states represent a conducting system with very high normal conductivity because of protection against time-reversal-invariant scattering mechanisms. Therefore, it is of great interest to understand the nature and origin of the charge carriers that underlie this interfacial superconductivity, and in particular, to see if the topologically-protected surface states might be a source of the normal carriers. The relevance of this question is broader than the specific system studied here, since it has been recently proposed that interfacial superconductivity may even play a role in cuprates: for example, in the interface located between charge density wave nanoscale puddles [42] and between oxygen-rich grains where the interface is made of a filamentary network with hyperbolic geometry [43,44]. We describe below how the current-induced depairing approach was used to answer these questions to elucidate the nature of the normal state in the $\text{Bi}_2\text{Te}_3/\text{FeTe}$ system.

4.2. Samples and Experimental Information

The Bi₂Te₃/FeTe samples consisted of a ZnSe buffer layer (50 nm) deposited on a GaAs (001) semi-insulating substrate, followed by a deposition of 220 nm thick FeTe, which was then capped with a 20 nm-thick Bi₂Te₃ layer. Upper-critical-field measurements [41] and vortex-explosion measurements [45] showed that the superconductivity occurred within an interfacial layer of thickness $d = 7$ nm, which was much thinner than both the FeTe and Bi₂Te₃ layers. Projection photolithography followed by argon-ion milling was used to pattern narrow microbridges optimized for the high current-density pulsed four-probe measurements. Two bridges were studied: Sample A with lateral dimensions of width $w = 11.5$ μm and length $l = 285$ μm and Sample B with $w = 12$ μm and $l = 285$ μm . The onset T_c (defined as the intersection of the extrapolation of the normal-state portion and the extrapolation of the steep transition portion of the $R(T)$ curve) for both bridges, was 11.7 K. Details about sample preparation are provided in [41]. All measurements were made in zero applied magnetic field. While the very low reference curves at $I \leq 60$ μA were measured using continuous DC signals, the main electrical transport measurements were made with pulsed signals. Contact resistances (<1 Ω) were much lower than the normal resistance R_n of the bridge, and heat generated at contacts did not reach the bridge within the time duration t of each pulse, since the thermal diffusion distance ($\sqrt{Dt} \sim 10$ μm) was much shorter than the contact-to-bridge distance (>1 mm); here, D is the diffusion constant.

4.3. Results and Discussion

The normal-state resistivity $\rho_n(T)$ and depairing current density $j_d(T)$ in the Bi₂Te₃/FeTe samples were extracted over the entire temperature range [46], by driving the system normal with high pulsed currents using the methods described earlier and illustrated in Figures 4 and 5. Figure 7 shows the raw depairing current results. The dashed horizontal lines in Panels (a) and (b) provide the values $I_d(T \rightarrow 0) \geq 0.131$ A and 0.136 A for Samples A and B, respectively.

In order to obtain more accurate intrinsic j_d and ρ_n of the 7 nm-thick superconducting interfacial layer itself, we needed to subtract the small parallel current through the normally conductive underlying FeTe layer. For this purpose, a separate measurement of pure FeTe deposited on ZnSe/GaAs, without the Bi₂Te₃ top layer, was conducted [46]. With this subtraction, the previous raw $I_d(T \rightarrow 0)$ values gave a corrected $j_d(T = 0)$ of 1.5×10^8 A/cm² for both samples (which is a typical value: j_d ranges 10^7 – 10^9 A/cm² for most superconductors), and the correction gave the intrinsic $\rho_n(T)$ for the two samples, as shown in Figure 8. This absolute value of $\rho_n(T \rightarrow 0) \sim 200$ n Ω cm represents an extraordinarily conductive normal state for a superconducting system, as most superconductors are poor conductors in the normal state. This information will be analyzed below within the framework of an anisotropic Ginzburg–Landau (GL) approach [46], to obtain information on the superfluid density, carrier concentration, and scattering rate, as well as their implications for the nature of the normal-state.

From the previously-published measurements of He et al. [41], we have the following orientation-dependent values of B_{c2} : perpendicular-to-interface $B_{c2}^\perp(0) \approx 17$ T and parallel-to-interface $B_{c2}^\parallel(0) \approx 40$ T. The corresponding coherence lengths from Equation (3) are: in-plane $\xi_\parallel(0) \approx 4.4$ nm and perpendicular $\xi_\perp(0) \approx 1.9$ nm. Using Equation (23) together with this $B_{c2}^\perp(0)$ and our measured in-plane $j_d^\parallel(0)$ gave $\lambda_\parallel(0) = 124$ nm and a corresponding $\rho_s(0) = 1/\lambda_\parallel^2(0)$. From $\rho_s(0) = \mu_0 n_s(0) e^2 / m^* \approx \mu_0 n e^2 / m$ applicable in the clean limit at $T = 0$, we get $n \approx 1.8 \times 10^{21}$ per cm³, approximating $m^* \approx m$. This effective single-band value of n evaluated above is similar to n characteristic of high temperature superconductors and about two orders of magnitude lower than n in highly-conductive metals such as copper.

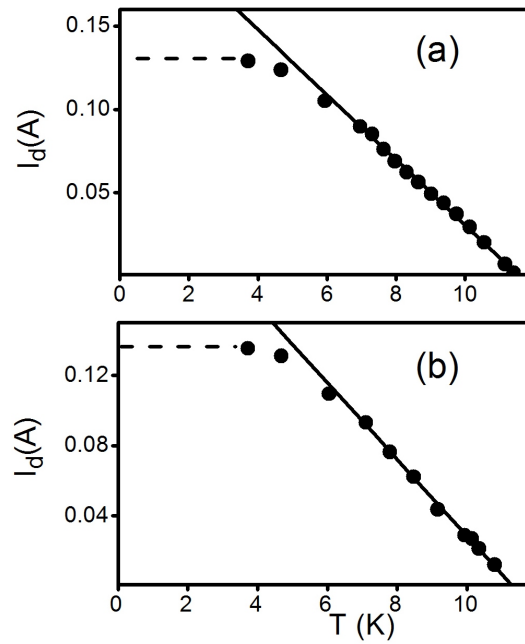


Figure 7. Raw depairing current versus temperature for $\text{Bi}_2\text{Te}_3/\text{FeTe}$ bridges: (a) Sample A and (b) Sample B. The dashed horizontal lines provide the values $I_d(T \rightarrow 0) \geq 0.131$ A and 0.136 A for Samples A and B, respectively (adapted from Reference [46]).

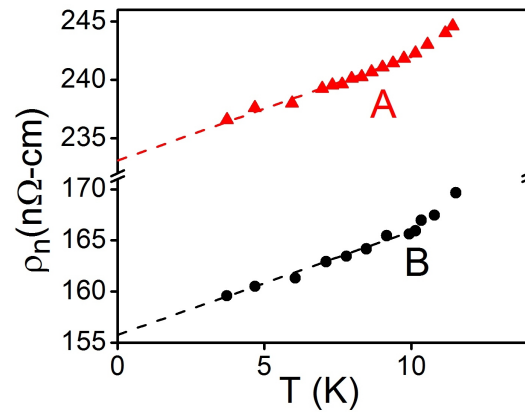


Figure 8. Intrinsic normal-state resistivity of $\text{Bi}_2\text{Te}_3/\text{FeTe}$ interfacial superconducting bridges, Samples A and B (adapted from Reference [46]).

The low value of n together with the very high normal conductivity implies a rather long scattering time τ and mean-free-path l . The Fermi wave number for this n computes to $k_F(3D) = m^*v_F/\hbar = (3\pi^2n)^{1/3} = 3.8 \times 10^9 \text{ m}^{-1}$ and $k_F(2D) = (2\pi nd)^{1/2} = 9.0 \times 10^9 \text{ m}^{-1}$ in three and two dimensions, respectively. In both cases, the Fermi wavelength $\lambda_F = 2\pi/k_F \ll d$, validating the continuum approximation for states along the perpendicular direction and justifying the anisotropic 3D treatment of the normal state. Then, from the Drude relationship $\rho \approx m/ne^2\tau$, we get $\tau \approx 10$ ps, which agrees well with the scattering rates ($\sim \hbar/0.05 \text{ meV} = 13$ ps) measured by Pan et al. [47] using spin- and angle-resolved photoemission spectroscopy. Combining this value of τ with the Fermi velocity $v_F = \hbar k_F/m \approx 440 \text{ km/s}$, we get $l = v_F\tau = 4.2 \text{ }\mu\text{m}$. The very long l , which well exceeds the superconducting layer thickness d , indicates that scattering from the faces that bound the superconducting layer was of a specular nature. This surprising dramatically low scattering indeed supports the possible role of the topological surface states in the formation of the normal state that underlies this exotic interfacial superconducting system.

5. Concluding Remarks

Fast pulsed signals of short duration and low duty cycle make it possible to study transport behavior in superconductors at extreme current densities, power densities, and electric fields. In this article, we focused on the use of this technique in the measurement of one of the fundamental critical parameters of the superconducting state, the depairing current j_d . It was shown how through j_d , one can obtain information on various other key parameters of the superconducting state, in particular the penetration depth and consequent superfluid density, which cast light on the normal state. As an example and illustration of this procedure, we described a recent study of the superconducting system formed at the interface between a topological insulator and a chalcogenide. We hope that the information provided here will encourage other groups to utilize this approach.

Funding: This work was supported by the U.S. Department of Energy through Grant Number DE-FG02-99ER45763.

Acknowledgments: The following are acknowledged for useful discussions and other assistance: Charles L. Dean, Manlai Liang, Gabriel F. Saracila, James M. Knight, Luc Fruchter, Ziang Z. Li, Qing Lin He, Hongchao Liu, Jiannong Wang, Rolf Lortz, Iam Keong Sou, Alex Gurevich, Richard A. Webb, Ken Stephenson, and David K. Christen.

Conflicts of Interest: The author declares no conflict of interest.

References

1. Onnes, K.H. Further experiments with liquid helium. C. On the change of electric resistance of pure metals at very low temperatures, etc. IV. The resistance of pure mercury at helium temperatures. In *Through Measurement to Knowledge*; Springer: Dordrecht, The Netherlands, 1911; pp. 261–263. [[CrossRef](#)]
2. Somayazulu, M.; Ahart, M.; Mishra, A.K.; Geballe, Z.M.; Baldini, M.; Meng, Y.; Struzhkin, V.V.; Hemley, R.J. Evidence for Superconductivity above 260 K in Lanthanum Superhydride at Megabar Pressures. *Phys. Rev. Lett.* **2019**, *122*, 027001–027004. [[CrossRef](#)] [[PubMed](#)]
3. Drozdov, A.P.; Kong, P.P.; Minkov, V.S.; Besedin, S.P.; Kuzovnikov, M.A.; Mozaffari, S.; Balicas, L.; Balakirev, F.; Graf, D.; Prakapenka, V.B.; et al. Superconductivity at 250 K in lanthanum hydride under high pressures. *Nature* **2019**, *569*, 528–531. [[CrossRef](#)] [[PubMed](#)]
4. Tinkham, M. *Introduction to Superconductivity*, 2nd ed.; Dover Publications: Mineola, NY, USA, 2004; ISBN-10: 0486435032, ISBN-13: 978-0486435039.
5. Emery, V.J.; Kivelson, S.A. Importance of phase fluctuations in superconductors with small superfluid density. *Nature* **1995**, *374*, 434–437. [[CrossRef](#)]
6. Uemura, Y.J.; Luke, G.M.; Sternlieb, B.J.; Brewer, J.H.; Carolan, J.F.; Hardy, W.N.; Kadono, R.; Kempton, J.R.; Kiefl, R.F.; Kreitzman, S.R.; et al. Universal Correlations between T_c and n_s/m^* (Carrier Density over Effective Mass) in High- T_c Cuprate Superconductors. *Phys. Rev. Lett.* **1989**, *62*, 2317–2320. [[CrossRef](#)] [[PubMed](#)]
7. Uemura, Y.J.; Le, L.P.; Luke, G.M.; Sternlieb, B.J.; Wu, W.D.; Brewer, J.H.; Riseman, T.M.; Seaman, C.L.; Maple, M.B.; Ishikawa, M.; et al. Basic similarities among cuprate, bismuthate, organic, Chevrel-phase, and heavy-fermion superconductors shown by penetration-depth measurements. *Phys. Rev. Lett.* **1991**, *66*, 2665–2668. [[CrossRef](#)] [[PubMed](#)]
8. Hardy, W.N.; Bonn, D.A.; Morgan, D.C.; Liang, R.; Zhang, K. Precision measurements of the temperature dependence of λ in $Y_1Ba_2Cu_3O_7$: Strong evidence for nodes in the gap function. *Phys. Rev. Lett.* **1993**, *70*, 3999–4002. [[CrossRef](#)] [[PubMed](#)]
9. Felcher, G.P.; Kampwirth, R.T.; Gray, K.E.; Felici, R. Polarized-Neutron Reflections: A New Technique Used to Measure the Magnetic Field Penetration Depth in Superconducting Niobium. *Phys. Rev. Lett.* **1984**, *52*, 1539–1542. [[CrossRef](#)]
10. Claassen, J.H.; Evetts, J.E.; Somekh, R.E.; Barber, Z.H. Observation of the superconducting proximity effect from kinetic-inductance measurements. *Phys. Rev. B* **1991**, *44*, 9605–9608. [[CrossRef](#)]
11. Yong, J.; Lee, S.; Jiang, J.; Bark, C.W.; Weiss, J.D.; Hellstrom, E.E.; Larbalestier, D.C.; Eom, C.B.; Lemberger, T.R. Superfluid density measurements of $Ba(Co_xFe_{1-x})_2As_2$ films near optimal doping. *Phys. Rev. B* **2011**, *83*, 104510–104514. [[CrossRef](#)]
12. Boghosian, C.; Meyer, H.; Rives, J.E. Density, Coefficient of Thermal Expansion, and Entropy of Compression of Liquid Helium-3 under Pressure below 1.2 K. *Phys. Rev.* **1966**, *146*, 110–119. [[CrossRef](#)]

13. Van Degrift, C.T. Tunnel diode oscillator for 0.001 ppm measurements at low temperatures. *Rev. Sci. Instr.* **1975**, *46*, 599. [[CrossRef](#)]
14. Sonier, J.E. Muon spin rotation studies of electronic excitations and magnetism in the vortex cores of superconductors. *Rep. Prog. Phys.* **2007**, *70*, 1717–1756. [[CrossRef](#)]
15. Luan, L.; Auslaender, O.M.; Lippman, T.M.; Hicks, C.W.; Kalisky, B.; Chu, J.-H.; Analytis, J.G.; Fisher, I.R.; Kirtley, J.R.; Moler, K.A. Local measurement of the penetration depth in the pnictide superconductor $\text{Ba}(\text{Fe}_{0.95}\text{Co}_{0.05})_2\text{As}_2$. *Phys. Rev. B* **2010**, *81*, 100501–100504. [[CrossRef](#)]
16. Shibauchi, T.; Kitano, H.; Uchinokura, K.; Maeda, A.; Kimura, T.; Kishio, K. Anisotropic penetration depth in $\text{La}_{2-x}\text{Sr}_x\text{CuO}_4$. *Phys. Rev. Lett.* **1994**, *72*, 2263–2266. [[CrossRef](#)]
17. Lee, J.Y.Y.; Lemberger, T.R. Penetration depth $\lambda(T)$ of $\text{Y}_1\text{Ba}_2\text{Cu}_3\text{O}_7$ films determined from the kinetic inductance. *Appl. Phys. Lett.* **1993**, *62*, 2419–2421. [[CrossRef](#)]
18. Saracila, G.F.; Kunchur, M.N. Ballistic acceleration of a supercurrent in a superconductor. *Phys. Rev. Lett.* **2009**, *102*, 077001–077004. [[CrossRef](#)] [[PubMed](#)]
19. Diener, P.; Leduc, H.G.; Yates, S.J. Design and Testing of Kinetic Inductance Detectors Made of Titanium Nitride. *J. Low Temp. Phys.* **2012**, *167*, 305–310. [[CrossRef](#)]
20. Jochem, B. Kinetic Inductance Detectors. *J. Low Temp. Phys.* **2012**, *167*, 292–304. [[CrossRef](#)]
21. Kunchur, M.N.; Dean, C.; Liang, M.; Moghaddam, N.S.; Guarino, A.; Nigro, A.; Grimaldi, G.; Leo, A. Depairing current density of $\text{Nd}_{2-x}\text{Ce}_x\text{CuO}_4$ superconducting films. *Physica C* **2013**, *495*, 66–68. [[CrossRef](#)]
22. Kunchur, M.N.; Ivlev, B.I.; Christen, D.K.; Phillips, J.M. Metallic Normal State of $\text{Y}_1\text{Ba}_2\text{Cu}_3\text{O}_7$. *Phys. Rev. Lett.* **2000**, *84*, 5204–5207. [[CrossRef](#)] [[PubMed](#)]
23. Larkin, A.I.; Ovchinnikov, Y.U.N. Nonlinear conductivity of superconductors in the mixed state. *Sov. Phys.—JETP* **1976**, *41*, 960–965.
24. Blatter, G.; Feigel'man, M.V.; Mikhail, V.B.; Larkin, A.I.; Valerii, V.M. Vortices in high-temperature superconductors. *Rev. Mod. Phys.* **1994**, *66*, 1125–1388. [[CrossRef](#)]
25. Kunchur, M.N. Unstable flux flow due to heated electrons in superconducting films. *Phys. Rev. Lett.* **2002**, *89*, 137005–137008. [[CrossRef](#)] [[PubMed](#)]
26. Kunchur, M.N. Current-induced pair breaking in Magnesium Diboride. *J. Phys. Condens. Matter.* **2004**, *16*, R1183–R1204. [[CrossRef](#)]
27. London, F.; London, H. The electromagnetic equations of the supraconductor. *Proc. Roy. Soc.* **1935**, *A149*, 71–88. [[CrossRef](#)]
28. Ginzburg, V.L.; Landau, L.D. On the Theory of superconductivity. *Zh. Eksperim. Teor. Fiz.* **1950**, *20*, 1064–1082.
29. Bardeen, J. Critical Fields and Currents in Superconductors. *Rev. Mod. Phys.* **1962**, *34*, 667–681. [[CrossRef](#)]
30. Romijn, J.; Klapwijk, T.M.; Renne, M.J.; Mooij, J.E. Critical pair-breaking current in superconducting aluminum strips far below T_c . *Phys. Rev. B* **1982**, *26*, 3648–3655. [[CrossRef](#)]
31. Maki, K. On Persistent Currents in a Superconducting Alloy. II. *Progr. Theor. Phys.* **1963**, *29*, 333–340. [[CrossRef](#)]
32. Ovchinnikov, Y.U.N. Critical current of thin films for diffuse reflection from the walls. *Sov. Phys.—JETP* **1969**, *29*, 853–860.
33. Kupriyanov, M.Y.; Lukichev, V.F. Temperature dependence of pair-breaking current in superconductors. *Sov. J. Low Temp. Phys.* **1980**, *6*, 210.
34. Bauer, E.; Paul, C.; Berger, S.; Majumdar, S.; Michor, H.; Giovannini, M.; Saccone, A.; Bianconi, A. Thermal conductivity of superconducting MgB_2 . *J. Phys. Condens. Matter* **2001**, *13*, L487–L493. [[CrossRef](#)]
35. Agrestini, S.; Metallo, C.; Filippi, M.; Simonelli, L.; Campi, G.; Sanipoli, C.; Liarokapis, E.; De Negri, S.; Giovannini, M.; Saccone, A.; et al. Substitution of Sc for Mg in MgB_2 : Effects on transition temperature and Kohn anomaly. *Phys. Rev. B* **2004**, *70*, 134514–134518. [[CrossRef](#)]
36. Kagan, M.Y.; Bianconi, A. Fermi-Bose Mixtures and BCS-BEC Crossover in High- T_c Superconductors. *Condens. Matter* **2019**, *4*, 51. [[CrossRef](#)]
37. Kunchur, M.N.; Christen, D.K.; Klabunde, C.E.; Phillips, J.M. Pair-breaking effect of high current densities on the superconducting transition in $\text{Y}_1\text{Ba}_2\text{Cu}_3\text{O}_7$. *Phys. Rev. Lett.* **1994**, *72*, 752–75.
38. Liang, M.; Kunchur, M.N.; Fruchter, L.; Li, Z.Z. Depairing current density of infinite-layer $\text{Sr}_{1-x}\text{La}_x\text{CuO}_2$ superconducting films. *Physica C* **2013**, *492*, 178–180. [[CrossRef](#)]
39. Werthamer, N.R.; Helfand, E.; Hohenberg, P.C. Temperature and Purity Dependence of the Superconducting Critical Field, H_{c2} . III. Electron Spin and Spin-Orbit Effects. *Phys. Rev.* **1966**, *147*, 295–302. [[CrossRef](#)]

40. Gurevich, A. Enhancement of the upper critical field by nonmagnetic impurities in dirty two-gap superconductors. *Phys. Rev. B* **2003**, *67*, 184515–184527. [[CrossRef](#)]
41. He, Q.L.; Liu, H.; He, M.; Lai, Y. H.; He, H.; Wang, G.; Law, K.T.; Lortz, R.; Wang, J.; Sou, I.K. Two-dimensional superconductivity at the interface of a Bi₂Te₃/FeTe heterostructure. *Nat. Commun.* **2014**, *5*, 4247–4254. [[CrossRef](#)]
42. Campi, G.; Bianconi A.; Poccia, N.; Bianconi, G.; Barba, L.; Arrighetti, G.; Innocenti, D.; Karpinski, J.; Zhigadlo, N. D.; Kazakov, S. M.; et al. Inhomogeneity of charge-density-wave order and quenched disorder in a high-*T_c* superconductor. *Nature* **2015**, *525*, 359–362. [[CrossRef](#)]
43. Jarlborg, T.; Bianconi A. Multiple Electronic Components and Lifshitz Transitions by Oxygen Wires Formation in Layered Cuprates and Nickelates. *Condens. Matter* **2019**, *4*, 15. [[CrossRef](#)] [[PubMed](#)]
44. Campi, G.; Bianconi A. High Temperature superconductivity in a hyperbolic geometry of complex matter from nanoscale to mesoscopic scale. *J. Supercond. Nov. Magn.* **2016**, *29*, 627–631. [[CrossRef](#)]
45. Dean, C.L.; Kunchur, M.N.; He, Q.L.; Liu, H.; Wang, J.; Lortz, R.; Sou, I.K. Current driven vortex-antivortex pair breaking and vortex explosion in the Bi₂Te₃/FeTe interfacial superconductor. *Physica C* **2016**, *527*, 46–49. [[CrossRef](#)]
46. Dean, C.L.; Kunchur, M.N.; He, Q.L.; Liu, H.; Wang, J.; Lortz, R.; Sou, I.K. Current-induced depairing in the Bi₂Te₃/FeTe interfacial superconductor. *Phys. Rev. B* **2015**, *92*, 094502–094506. [[CrossRef](#)]
47. Pan, Z.-H.; Fedorov, A.V.; Gerdner, D.; Lee, Y.S.; Chu, S.; Valla, T. Measurement of an Exceptionally Weak Electron-Phonon Coupling on the Surface of the Topological Insulator Bi₂Se₃ Using Angle-Resolved Photoemission Spectroscopy. *Phys. Rev. Lett.* **2012**, *108*, 187001–187005. [[CrossRef](#)]



© 2019 by the author. Licensee MDPI, Basel, Switzerland. This article is an open access article distributed under the terms and conditions of the Creative Commons Attribution (CC BY) license (<http://creativecommons.org/licenses/by/4.0/>).